Geophysical Journal International

Geophys. J. Int. (2018) **213,** 1121–1134
Advance Access publication 2018 January 23
GJI Seismology

doi: 10.1093/gji/ggy016

Abundant aftershock sequence of the 2015 M_w7.5 Hindu Kush intermediate-depth earthquake

Chenyu Li,[1] Zhigang Peng,[1] Dongdong Yao,[1] Hao Guo,[2] Zhongwen Zhan[3] and Haijiang Zhang[2]

[1] *School of Earth & Atmospheric Sciences, Georgia Institute of Technology, Atlanta, GA, USA. E-mail: lchenyu@gatech.edu*
[2] *School of Earth and Space Sciences and Laboratory of Seismology and Physics of Earth's Interior, University of Science and Technology of China, Hefei, China*
[3] *Seismological Laboratory, California Institute of Technology, Pasadena, CA, USA*

Accepted 2018 January 16. Received 2017 December 30; in original form 2017 July 17

SUMMARY

The 2015 M_w7.5 Hindu Kush earthquake occurred at a depth of 213 km beneath the Hindu Kush region of Afghanistan. While many early aftershocks were missing from the global earthquake catalogues, this sequence was recorded continuously by eight broad-band stations within 500 km. Here we use a waveform matching technique to systematically detect earthquakes around the main shock. More than 3000 events are detected within 35 d after the main shock, as compared with 42 listed in the Advanced National Seismic System catalogue (or 196 in the International Seismological Centre catalogue). The aftershock sequence generally follows the Omori's law with a decay constant $p = 0.92$. We also apply the recently developed double-pair double-difference technique to relocate all detected aftershocks. Most of them are located to the west of the hypocentre of the main shock, consistent with the westward propagation of the main-shock rupture. The aftershocks outline a nearly vertical southward dipping plane, which matches well with one of the nodal planes of the main shock. We conclude that the aftershock sequence of this intermediate-depth earthquake shares many similarities with those for shallow earthquakes and infer that there are some common mechanisms responsible for shallow and intermediate-depth earthquakes.

Key words: Earthquake interaction, forecasting, and prediction; Seismicity and tectonics; Statistical seismology; Subduction zone processes.

1 INTRODUCTION

Earthquakes with hypocentral depth greater than 70 km are termed as deep earthquakes, and further divided into intermediate-depth earthquakes between 70 and 300 km, and deep-focus earthquakes below 300 km (Wadati 1928; Frohlich 1989, 2006; Houston 2015). Intermediate-depth and deep-focus earthquakes mostly occur along subduction plate boundaries, forming the so-called Wadati–Benioff zones (Wadati 1928; Frohlich 1989). The deepest recorded earthquakes are close to the bottom of mantle transition zone at ~700 km (Houston 2015; Ye *et al*. 2016). Although intermediate-depth earthquakes generally produce less shaking than shallow earthquakes with similar magnitudes due to their larger depths, they are widely felt at greater distances from the epicentre. Some of them could cause damages, especially in regions without strict building codes (Frohlich 2006).

Seismic radiation and focal mechanism of deep earthquakes indicate predominant shear failure plane, consistent with double couple mechanism and similar to shallow earthquakes (Green & Houston 1995; Wiens 2001; Green & Marone 2002; Houston 2015; Ye *et al*. 2016). Yet deep earthquakes show many differences in focal mechanisms and statistical properties. For example, they have clear non-double-couple components and their *b*-values and aftershock productivities show large variations in different regions (e.g. Houston 2015; Poli *et al*. 2016a,b; Zhan 2017). Furthermore, deep earthquakes occur well below depths where brittle failures would occur, requiring alternative weakening mechanisms (Green & Houston 1995; Frohlich 2006). At present, the underlying physical mechanisms of deep earthquakes are still under debate (e.g. Houston 2015). These include dehydration embrittlement (Rayleigh & Paterson 1965; Petit & Barquins 1988; Houston 2015), transformational faulting (Green & Houston 1995; Kirby *et al*. 1996; Houston 2015), and thermal shear instability (Ogawa 1987; Hobbs & Ord 1988; Karato *et al*. 2001; Poli *et al*. 2016a).

Detailed observations of deep earthquake sequences can be used to constrain their physical models (e.g. Zhan 2017). For example, earlier studies demonstrated that deep earthquakes typically have lower aftershock productivity than shallow earthquakes, suggesting different nucleation/rupture processes (Kagan & Knopoff 1980; Prozorov & Dziewonski 1982; Frohlich 1987; Persh & Houston

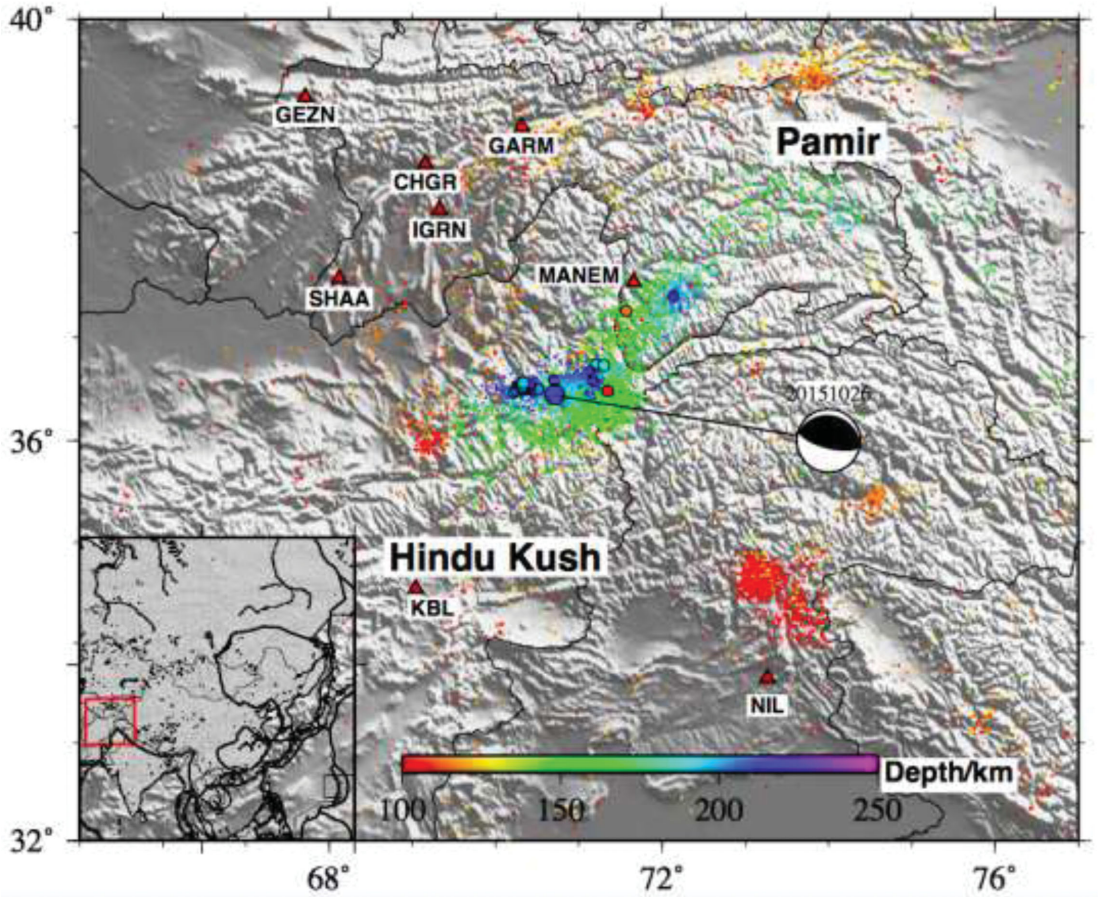

Figure 1. Map showing the study region around Hindu Kush. Earthquakes are sized according to their magnitudes. Coloured dots are background seismicity since 2000 and their hypocentral depths are indicated by the colour. The red triangles are stations used in this study. Inset shows the location of Pamir–Hindu Kush region, and black thick line indicates plate boundaries.

2004; Poli *et al*. 2016a,b). However, at least some deep earthquakes were followed by abundant aftershock sequences decaying with the Omori's Law, such as the March 1994 Tonga deep earthquake (Wiens *et al*. 1994; Nyffeneger & Frohlich 2000). That sequence could be a rare case, because it was well recorded by an eight-broad-band station array around the epicentre, while most deep earthquakes remain poorly covered by regional or global seismic networks. Hence, it is still not clear whether the relative lack of aftershocks is real, or due to the paucity of near-field recordings.

It is well known that global/regional earthquake catalogues are incomplete immediately after a large shallow earthquake, mainly due to overlapping events with high seismicity rate or the masking of coda wave from the main shock and large aftershocks (Kagan 2004; Peng *et al*. 2007; Iwata 2008). Although no detailed investigation of early aftershock completeness following large deep earthquakes was performed before, we expect that at least some deep aftershocks could be missing for the same reason. It is important to detect those missing early aftershocks for deep earthquakes, because they not only help to define main-shock rupture plane, but also provide important clues on possible physical mechanisms (Wiens *et al*. 1994; Houston 2015).

An effective way to detect missing smaller-magnitude events from conventional catalogues is the waveform matched-filter technique (WMFT; Gibbons & Ringdal 2006; Shelly *et al*. 2007; Peng & Zhao 2009). It utilizes waveforms and travel time information of known events as templates, or 'matched filters' (Shearer 1994), to search for similar patterns in the continuous recordings. WMFT has been successfully applied to detect missing earthquakes before (e.g. Kato *et al*. 2012; Kato & Nakagawa 2014; Walter *et al*. 2015; Ruan *et al*. 2017) and after large shallow earthquakes (Peng & Zhao 2009; Meng *et al*. 2013; Meng & Peng 2014), as well as low-frequency earthquakes within deep tectonic tremors (e.g. Shelly *et al*. 2007; Brown *et al*. 2008; Shelly & Hardebeck 2010; Tang *et al*. 2010; Frank & Shapiro 2014; Chao *et al*. 2017).

In this study, we apply the WMFT to the 2015 M_w7.5 intermediate-depth earthquake sequence in the Hindu Kush region of Afghanistan. We choose this sequence, mostly because several broad-band stations are located within 500 km distances in Afghanistan and neighbouring countries (Fig. 1). In addition, the main-shock slip distribution (http://earthquake.usgs.gov/earthquakes/eventpage/us10003re5#finite-fault, USGS, last accessed 06/2016), its sub-event characteristics and rupture process (Zhan & Kanamori 2016; Poli *et al*. 2016a) are available, allowing us to compare our detection results with the main-shock behaviours to better understand this sequence and general behaviours of intermediate-depth earthquake sequences.

2 STUDY REGION

The Pamir–Hindu Kush seismic zone (Fig. 1) is located in the western syntaxis of Himalayas, a region with abundant

intermediate-depth earthquakes. The seismicity beneath Hindu Kush mostly occurs in the depth range of 70–250 km, and is slightly deeper than the Pamir region (Fig. 1). Relocated seismicity in both regions generally outlines a steeply northward dipping structure beneath Hindu Kush, and a southward dipping under Pamir (Pegler & Das 1998; Negredo *et al*. 2007; Sippl *et al*. 2013). It is still under debate whether there is a single contorted slab or two subducting slabs under the Pamir and Hindu Kush (Billington *et al*. 1977; Vinnik *et al*. 1977; Chatelain *et al*. 1980; Roecker *et al*. 1980; Hamburger *et al*. 1992; Negredo *et al*. 2007; Sippl *et al*. 2013; Kufner *et al*. 2016; Kufner *et al*. 2017). Pavlis & Hamburger (1991) showed that there were a small percentage (3 out of 40) of moderate-to-large ($M > 5.6$) intermediate-depth earthquakes having clear aftershock sequences in Hindu Kush. For some large events without clear aftershock sequences, they suggested that their aftershocks might be too small to be detected.

On 2015 October 26, an M_w 7.5 earthquake occurred at the depth of 213 km in the Hindu Kush region of Afghanistan, causing significant damages and casualties. There are recurring $M_w > 7$ intermediate depth earthquakes in the Hindu Kush region every 10–15 yr, and the previous one was an M_w7.4 earthquake on March 2002 with a close hypocentral location (Zhan & Kanamori 2016; Poli *et al*. 2016a). The USGS and Global CMT focal mechanism solutions for the 2015 event showed either a nearly vertical reverse or shallowly dipping thrust fault. Poli *et al*. (2016a) found that the main shock has two rupture stages: a ∼10 s precursory event with small *P*-wave amplitude, and a larger *P*-wave onset. These two stages indicated clear changes in rupture direction and energy radiation. Zhan & Kanamori (2016) determined four subevents for this main shock: the second and third subevents are to the west of epicentre, while the forth one is to the east. They also mentioned that the surface tectonic loading (∼1 cm yr^{-1}) cannot explain the short occurrence intervals for $M_w > 7$ earthquakes in Hindu Kush (∼10 cm yr^{-1}). Instead, these large earthquakes could be loaded by slab internal deformation (Lister *et al*. 2008).

3 DATA AND ANALYSIS PROCEDURE

We download continuous waveform 3 d before and 35 d after the 2015 M_w7.5 Hindu Kush earthquake recorded by eight nearby broad-band stations with a distance ranging from 80 to 500 km of networks IU and TJ from the IRIS Data Management Center (DMC). Two of the eight broad-band stations (Fig. 1) record continuously with a sampling rate of 40 Hz (BH), while the rest record with 100 Hz (HH). A visual inspection of high-pass filtered waveforms and spectrogram reveals numerous aftershocks within the first hour after the main shock (Fig. 2). The corresponding sound by speeding up the playback 100 times (Kilb *et al*. 2012) also reveals double distinct arrivals, corresponding to *P* and *S* waves of intermediate-depth events (Supporting Information Movie S1). The earliest aftershock listed in the Advanced National Seismic System (ANSS) catalogue is an M4.8 event around 40 minutes after the main shock, indicating that many early aftershocks were not listed in this global catalogue.

The analysis procedure of the WMFT generally follows Meng *et al*. (2013) and is briefly described here. We select 132 events between 2015 May 20 and 2015 December 31 listed in the ANSS catalogue as templates with inter-event distances less than 10° relative to the M_w7.5 main shock, and depth between 70 and 400 km. Both template and continuous waveforms are band-pass filtered at 2–8 Hz, because this frequency range has relatively good signal to noise ratios (SNRs) and is capable of suppressing most of the mainshock coda after a few hundred seconds (Fig. 2b). We manually pick the *P*/*S* phase arrivals for each template and compute the SNR for each trace, which is defined as the ratio between the cumulative energy for the signal (template) window (either *P* or *S* wave) and noise window (same length as the signal window ending 1 s before *P* wave). Following Li *et al*. (2017), the template windows are set to be 1 s before and 5 s after *P* wave arrival, and 1 s before and 11 s after arrival of *S* wave for three components of each station. Only template events containing at least 3 windows with SNR above 5 are used in further detection. We also down-sample the band-pass filtered waveforms to 0.05 s (20 Hz) to reduce the computational cost, and calculate the cross-correlation (CC) functions for selected *P* and *S* windows. Then we stack all CC functions after shifting them to the origin time of the template event, and output positive detections above a certain threshold. This is defined as the median CC value plus nine times median absolute deviation (MAD) of the stacked daily trace (Peng & Zhao 2009). Duplicated detections from multiple templates within a short time window are removed by keeping only the highest detection in every 12 s. The location of the newly detected event is initially assigned as the location of the best-matched template, and the magnitude is calibrated by the median peak amplitude ratio (Peng & Zhao 2009). Fig. 3 shows a positive detection (with inferred magnitude of 4.57) occurred 1184 s after the main shock with a mean CC value of 0.626 (∼33 times the MAD), and the corresponding template occurred on 2015/10/26 16:47:21 UTC, with a magnitude of 4.50.

In our previous studies (e.g. Meng *et al*. 2013; Li *et al*. 2017; Ruan *et al*. 2017; Wu *et al*. 2017, etc.), we simply assigned the location of the best-matching template to the newly detected event. This is valid to some degree since only nearby events could match the templates with high CCs. However, unless the mean CC value is 1, there are always minor time differences between the highest CC value of each trace and the stacked CC trace (i.e. the origin time of detected event), indicating small spatial offsets between the template and detected events (Supporting Information Fig. S1a). Such time shifts in turn can be used to relocate newly detected events with respect to the template events (e.g. Shelly *et al*. 2013; Zhang & Wen 2015).

Here we apply the newly developed double-pair double difference (DD) location algorithm (Guo & Zhang 2017; Guo *et al*. 2017) to relocate all detected earthquakes and template events. By making use of both station-pair and double-pair differential times with a hybrid strategy, this location method can improve both absolute and relative earthquake locations at the same time, as compared to the traditional event-pair DD relative location method (i.e. hypoDD; Waldhauser & Ellsworth 2000). Here we cut waveforms of all detected events, and compute CC differential times between pairs of events using a 3 s window (1 s before and 2 s after) around the *P* and *S* arrival time for each event. We only use event pairs containing at least 4 differential times with CC coefficients higher than 0.75. Example of two events with 4 differential times is shown in Supporting Information Fig. S1b.

As mentioned before, the initial locations of the detected events are assigned as the best-matched templates. We then construct double-pair data for all events using the aforementioned computed CC differential times. In order to better constrain the absolute locations, we also include the station-pair differential times from *P* and *S* arrivals for selected 550 events with SNR > 50, and relocate all events in the double-pair DD algorithm. The *P* wave velocity model is modified from a 1-D layered model (Sippl *et al*. 2013) and converted to a 1-D gradient model (Supporting Information Fig. S2), with a Vp/Vs ratio of 1.74 to estimate the *S*-wave velocity.

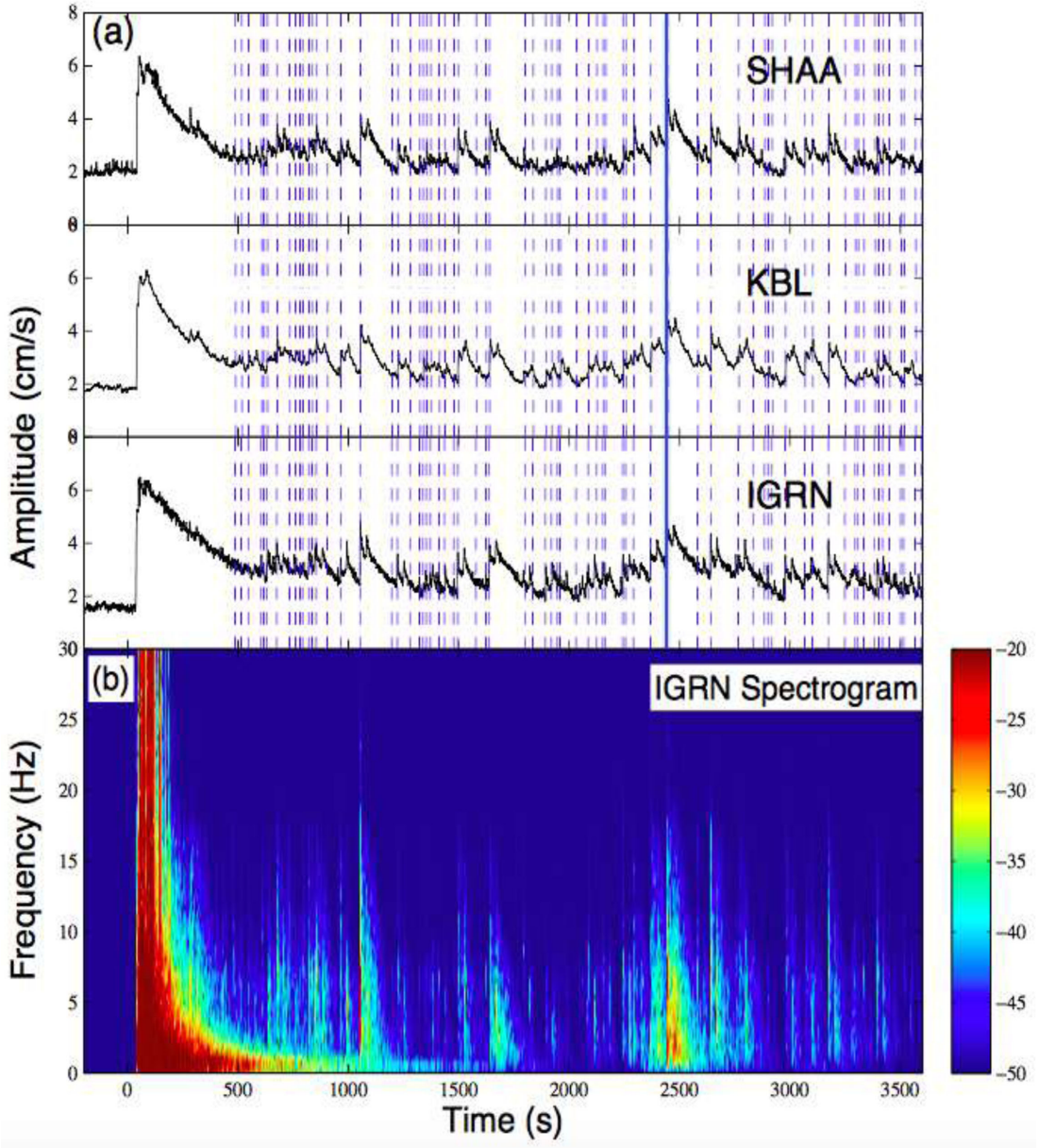

Figure 2. (a) Envelope function of 2–8 Hz bandpass filtered waveform of stations SHAA, KBL and IGRN, respectively. Solid blue line represents the M4.8 event on the ANSS catalogue, and dashed blue lines are all detected events with 9MAD by the WMFT within the first hour. (b) Spectrogram of station IGRN.

4 RESULTS

4.1 Event detection

By scanning through continuous waveforms 3 d before and 35 d after the 2015 Hindu Kush main shock with 132 templates, we detect 3120 events, including 1752 events in the first 3 d after the main shock above the threshold of 9 × MAD. In comparison, only 7 events are detected 3 d before the main shock, and only 42 and 196 aftershocks are listed in the ANSS and the International Seismological Centre (ISC) catalogue, respectively. After double-pair DD relocation, we obtained 1911 events with relative location uncertainties smaller than 5 km in three dimensions (Table 1).

In the newly detected catalogue, an M 5.32 event occurred on 2015 October 26, ∼2400 s after the main shock, which was not listed in the ANSS catalogue. The template event had a magnitude of 4.1 and occurred on 2015/11/12. The mean CC value is 0.115, just above 10 times the MAD. It is clear from the continuous waveform that one event did occur at the detection time (Supporting Information Fig. S3). To evaluate the accuracy of magnitude calibration, we compare the magnitudes of template events detected from other templates (after removing self-detection) and those listed in the ANSS catalogue (Peng & Zhao 2009). As shown in Supporting Information Fig. S4, the magnitude differences generally follow the tenfold relationship with median amplitude ratios, indicating that the magnitudes of template events are consistent.

4.2 Aftershock statistics

Fig. 4(a) shows the magnitudes versus logarithmic times following the main shock for the detected catalogue. It is evident that our detection capability increases with time, likely due to masking effect by the main-shock coda and large aftershocks at earlier times.

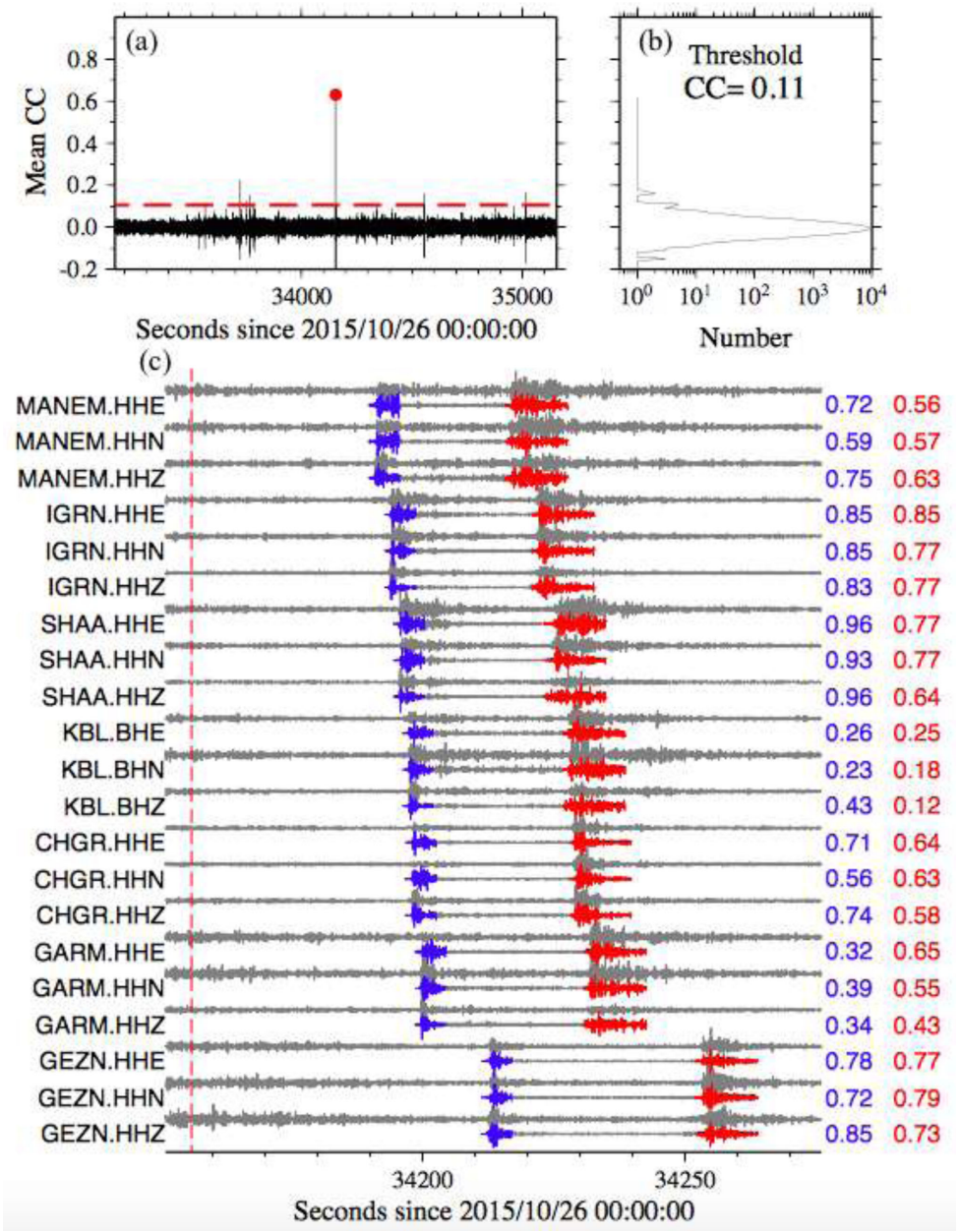

Figure 3. Example of a positive detection by an M4.5 template occurred on 2015/10/26 16:47:21. (a) Mean cross-correlation coefficient (CC) trace since 2015/10/26 00:00:00, the red dot represents the detected event plotted in panel (c), and the red dashed line is threshold of detected events (9MAD). (b) Histogram of the mean CC trace. (c) Comparison of continuous data and template in the matched time: blue traces are *P*-wave windows, red traces are *S*-wave windows of the template event, STATION.CHANNEL and CC values are labelled on left and right side, respectively.

Table 1. Detailed information of detected and relocated events.

	Event magnitude			Relative location uncertainty	
Number of events detected	>2.5	>3.1	Number of events relocated	<10 km	<5 km
3120	1391	519	2234	2086	1911

We use the ZMAP software (Wiemer 2001) to perform statistical analysis of the detected catalogue. The maximum curvature method (Woessner & Wiemer 2005) yields a magnitude of completeness *Mc* of 2.7 for the entire sequence, and $b = 0.73$ for the Gutenberg-Ritcher frequency-magnitude distribution (Figs 4a and b). We also apply a rate-dependent algorithm (Hainzl 2016) to estimate a varying *Mc*, and find that the *Mc* starts as 4.6 at ∼0.03 d (∼2600 s) after the main shock, and decreases to 2.7 around 1 d after main shock. If we use a constant $Mc = 2.7$, the aftershock rate would obey the Omori's law with a decaying constant $P = 0.92$ (Fig. 4c). To verify the robustness of our result, we also analyse the sequence using 12 × MAD as the cut-off threshold. It ends up with the same *Mc* of 2.7, and the corresponding *p* value is *0.95* (Supporting Information Fig. S5).

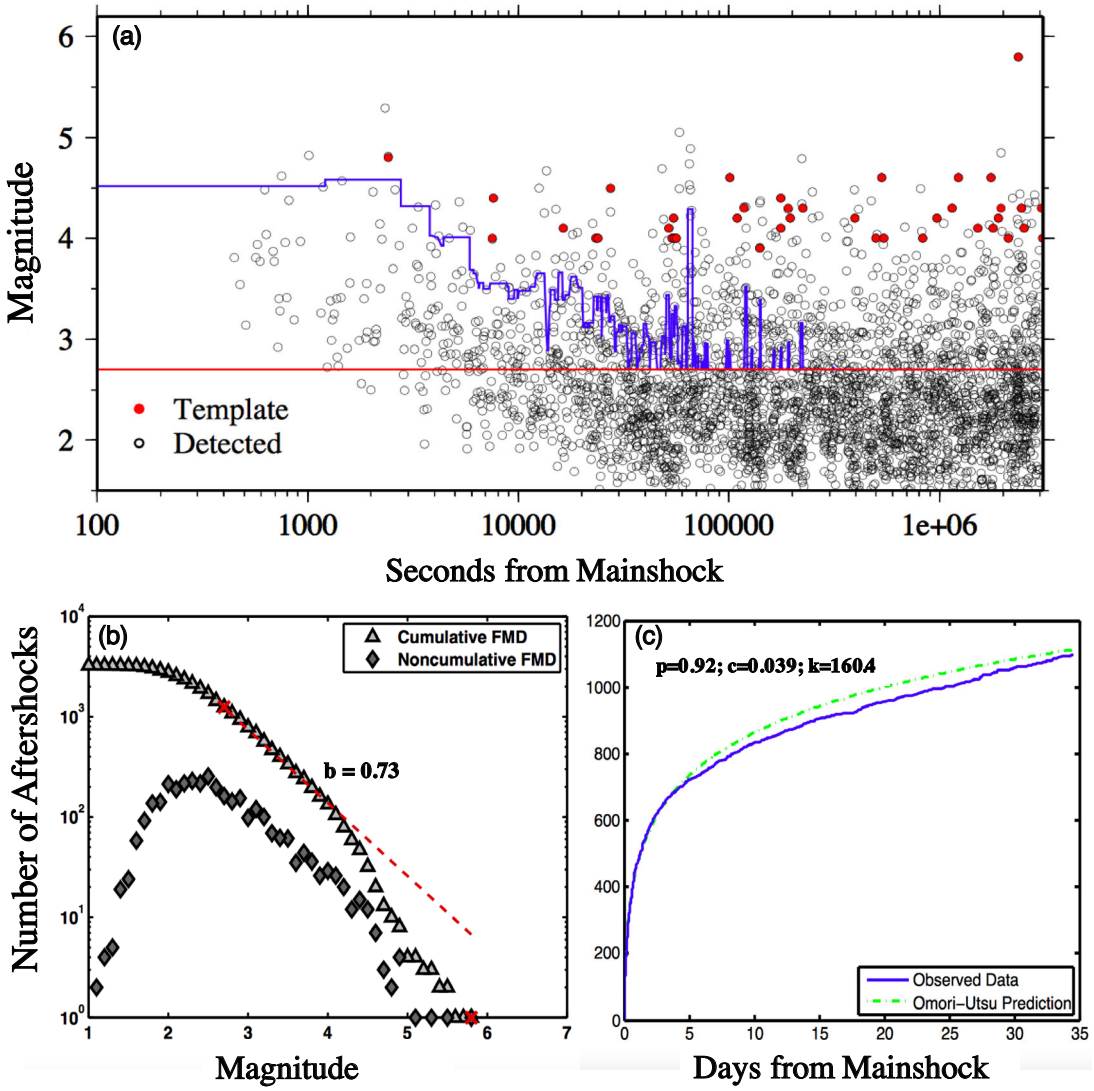

Figure 4. (a) Magnitude versus logarithmic time of detected events. Red dots and black circles are templates and detected events, respectively. The red solid line marks the Mc = 2.7, while blue solid line marks changing Mc after main shock. (b) Frequency–magnitude dependence for detected aftershocks generated by ZMAP, and the red dashed line indicates the result of 'Best Combination'. (c) Cumulative number of aftershocks in 35 d after the main shock, compared with the Omori–Utsu prediction.

4.3 Event relocation

Fig. 5 shows the spatial distribution of all relocated events and templates. It is clear that most aftershocks occurred to the west of main-shock hypocentre, near the edge of the large main-shock slip (Figs 5a and c). The aftershocks occurred in a near-vertical plane from 180 km to 230 km (Figs 5b and d). The cross-sections of seismicity are shown in Fig. 5(e), which delineate a near-vertical southward dipping plane. This is consistent with the general trend of south-dipping seismicity deeper than 180 km (Zhan & Kanamori 2016; Poli *et al*. 2016a; Kufner *et al*. 2017).

We find a moderate expansion of aftershocks with along-strike distances (Fig. 6). To better quantify this, we compute the activation time when the number of earthquakes within a small bin reaches to a certain threshold N (Kato & Obara 2014; Wu *et al*. 2017; Yao *et al*. 2017). Here we set the bin size as 5 km, and a sliding window of 1 km and $N = 20$. Fig. 6 shows that the activation time is at its minimum around 35 km west of the epicentre, and is migrating to two sides, with some smaller patches eastward being activated around 10^5 s after the main shock.

We use the bootstrapping method (Efron & Gong 1983; Efron & Tibshirani 1991) to quantify the relative location uncertainties of relocated seismicity for the target sequence from the double-pair DD location method (Guo & Zhang 2017; Guo *et al*. 2017). Both station-pair and double-pair differential times are randomly resampled in the bootstrapping method and are then used for the inversion with the same inversion procedure as for the real data. We repeat the process 50 times to obtain the standard deviation for each event. We calculate the median of the bootstrapping relative location uncertainties for all events, which help to suppress the effect of the outliers (Table 2). In general, the median relative location uncertainties are less than 0.2 and 0.6 km in horizontal and depth, respectively.

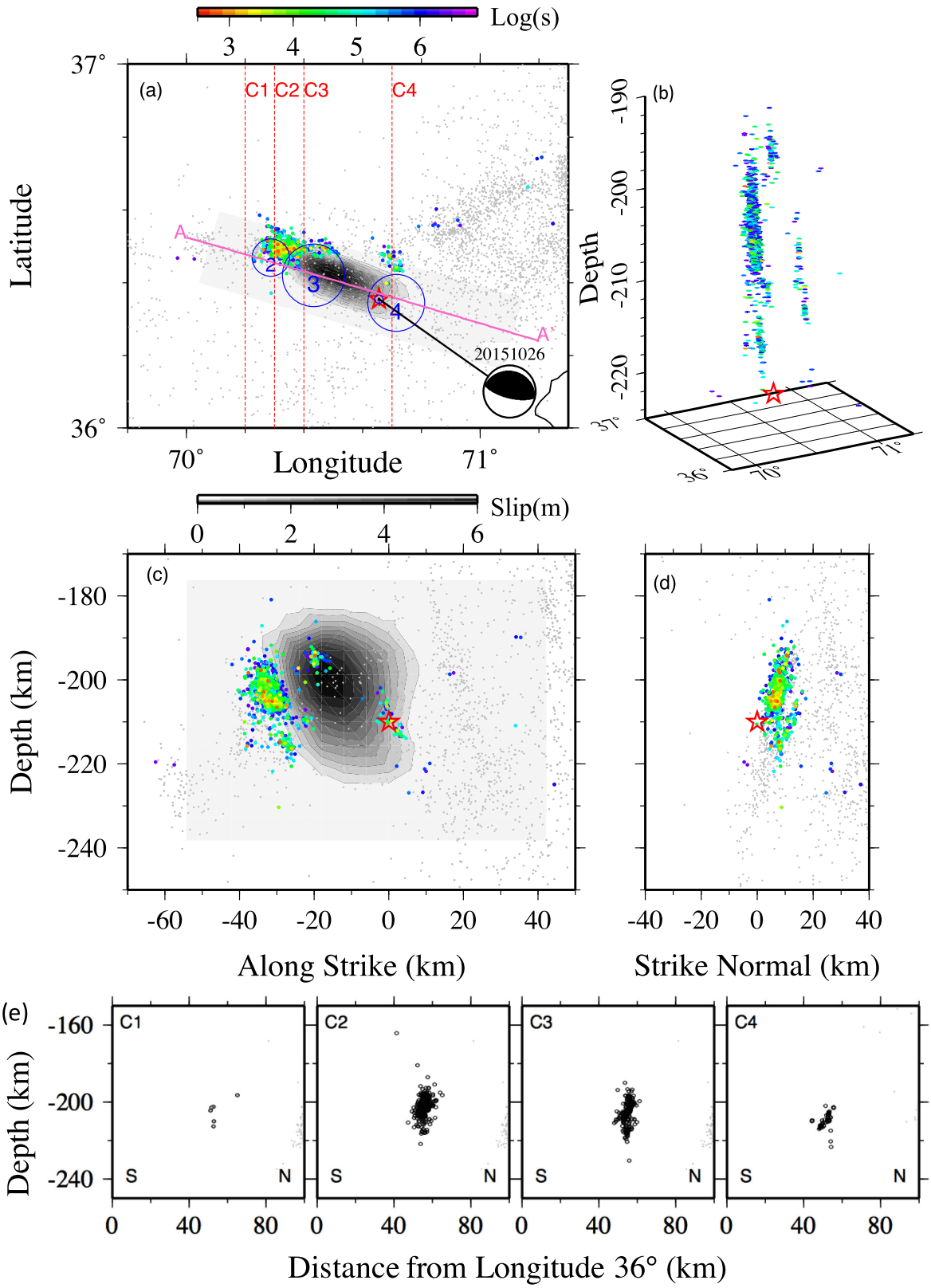

Figure 5. (a) Map view of detected aftershocks after relocation. The colour of aftershocks is their relative time to the main shock. The grey area and contours are slip distribution from finite fault model (USGS), after shifting the epicentre to the subevent 1 in Zhan & Kanamori (2016). Background seismicity between 2008–2010 and 2012–2014 are marked as grey dots (Kufner *et al* 2017), and blue circles mark subevents from Zhan & Kanamori (2016). Dashed red lines are cross-section profiles, AA' marks strike direction in panels (c) and (d). (b) 3-D view of aftershocks. Depth distribution of aftershocks (c) along and (d) perpendicular to strike. (e) Cross-sections of seismicity in panel (a) starting from longitude of 36°, seismicity within 5 km are projected.

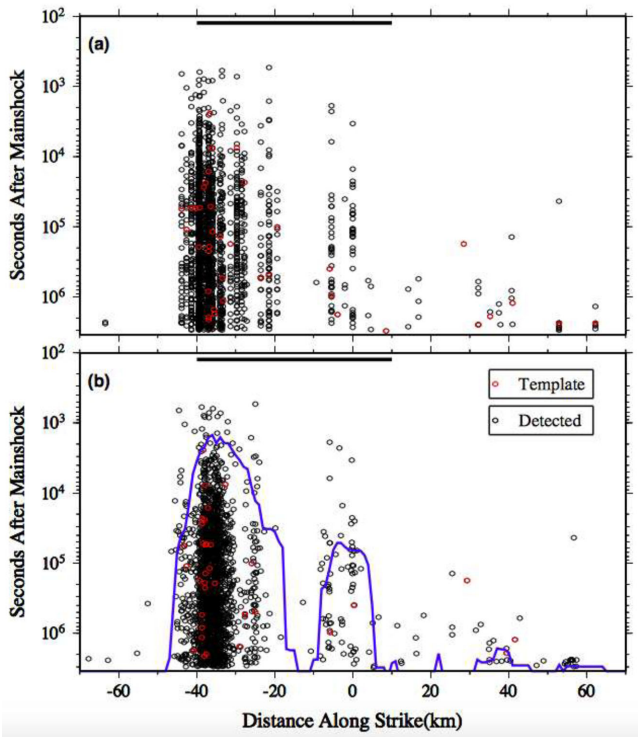

Figure 6. Distribution of aftershock along strike evolving with time (a) before and (b) after relocation. The red circles are template events and black circles are detected events, the thick black line represents the rupture region of main shock according to finite fault model, and the blue line marks activation time.

4.4 Comparisons with other catalogues

We compare our detection results with the ISC catalogue, and find 150 out of the 196 aftershocks within 35 d of the main shock from the ISC catalogue have time difference less than 6 s (Supporting Information Fig. S6a). The magnitudes of the detected catalogues are different when comparing with those listed in the ISC catalogue (Supporting Information Figs S6a and b). To investigate this further, we compare the magnitudes of events listed in both ANSS and ISC catalogues. There are some differences in magnitudes between the common events in the ANSS and ISC catalogues (Supporting Information Figs S6c and d). Thus, we believe the discrepancy of magnitudes mostly comes from the different magnitude sources in the ISC catalogue (Supporting Information Table S1).

Kufner *et al*. (2017) relocated some aftershocks of the 2015 Hindu Kush earthquake from the manually revisited quakeML files received from GEOFON earthquake bulletins with a master event method. We compare our relocated events with 20 aftershocks listed in Kufner *et al*. (2017) (Supporting Information Fig. S7). In both catalogues, aftershocks were mainly distributed to the west of main shock, while aftershocks in Kufner *et al*. (2017) were systematically ∼10 km shallower than our results. The discrepancy in depths might come from different initial locations and different location methods as well as velocity models between this study and Kufner *et al*. (2017) and will be further discussed in Sections 5.1 and 5.2.

Relocated aftershocks in this study, Poli *et al*. (2016a) and Kufner *et al*. (2017) all show that most aftershocks are located to the west of main shock and delineated a near-vertical south-dipping plane. A large portion of aftershocks located in this study were close to the second and third subevent from Zhan & Kanamori (2016), and concentrated in near-vertical south-dipping plane with width less than 20 km (Fig. 5). Due to the challenges of constraining the depths of these events, we did not directly compare the absolute location and depth of main-shock subevents and aftershocks in our study and others (Zhan & Kanamori 2016; Poli *et al*. 2016a; Kufner *et al*. 2017).

4.5 Aftershock productivity

As mentioned before, for many large deep earthquakes with well-recorded aftershock sequences, the numbers of aftershocks are small, generally less than 500 (Frohlich 2006; Prieto *et al*. 2012; Houston 2015). In this study we have detected more than 3000 aftershocks in the first 35 d following the 2015 Hindu Kush earthquake. To further quantify its aftershock productivity, we compare with shallow earthquakes and other deep earthquakes.

We first estimate the aftershock number from empirical equations given in Yamanake & Shimazaki (1990),

$$\log N = \tfrac{2}{3} \log M_0 - 17.05 \quad (1)$$

for shallow interplate earthquakes and

$$\log N = \tfrac{1}{2} \log M_0 - 12.08 \quad (2)$$

for shallow intraplate earthquakes. The estimated aftershock numbers are 8.92 and 26.30 for interplate and intraplate earthquakes respectively. We count our number of aftershocks with magnitudes larger than 4.5 in 30 d, and obtain $N = 16$. The above estimation suggests the aftershock productivity of 2015 Hindu Kush earthquake is comparable with that of shallow earthquakes.

We also compare the aftershock productivity with other deep earthquake sequences following a different approach. Persh & Houston (2004) defined a normalized number of aftershocks for deep earthquakes,

$$\log N_{\text{norm}} = \log N_{\text{obs}} + 8.2 - M_{\text{w}} Mw \quad (3)$$

Table 2. The median values of relative location uncertainties in three directions of all relocated events of the real data inversion, the noise-free synthetic test and the noisy synthetic test.

Location Uncertainty		*X* (km)	*Y* (km)	*Z* (km)
Relative location	Real data inversion	0.182	0.116	0.549
	Noise-free synthetic test	0.005	0.004	0.021
	Noisy synthetic test	0.229	0.166	0.731
	Initial error	2.052	1.144	2.810
Absolute location	Noise-free synthetic test	0.390	0.912	1.808
	Noisy synthetic test	0.500	0.967	2.200
	Initial error	3.1356	2.5114	5.3850

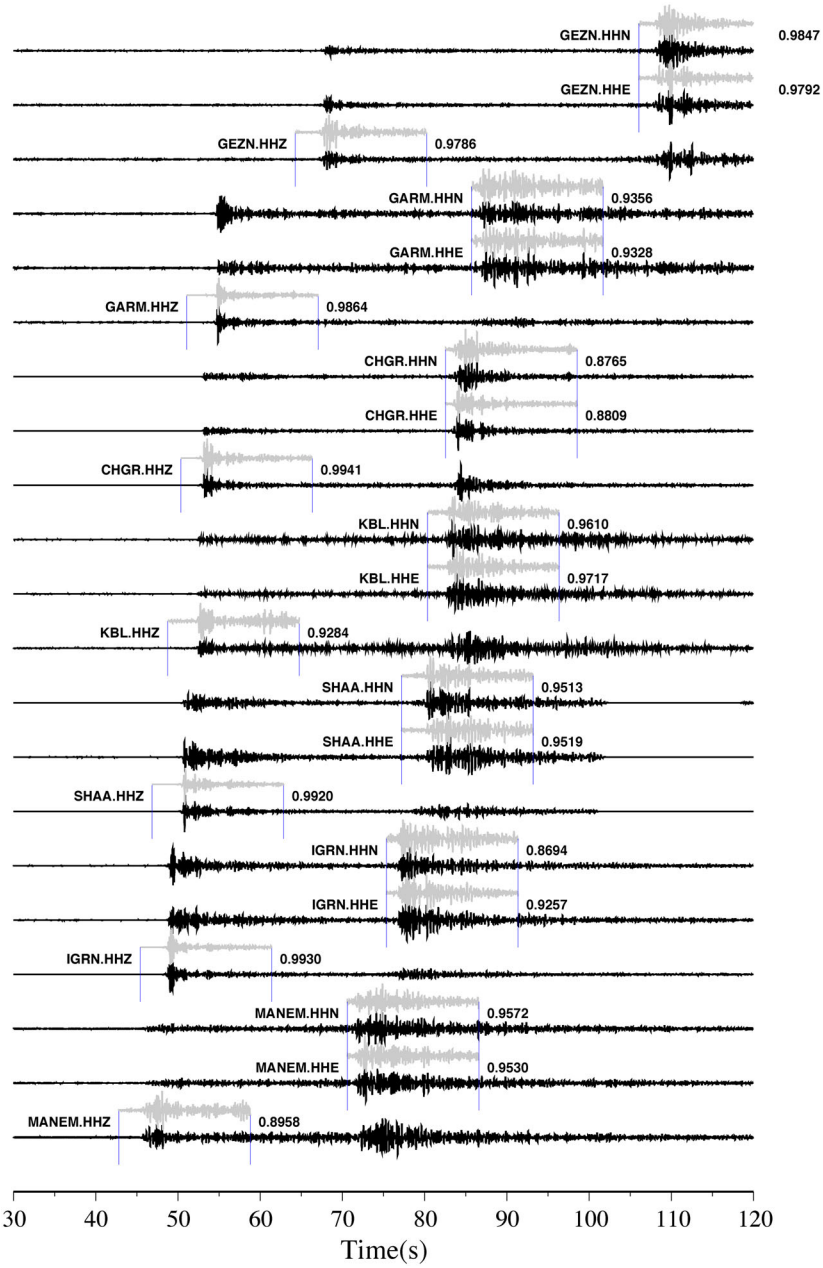

Figure 7. Waveforms of two repeating earthquakes, their origin time are 10/27/2015 03:09:02 and 10/29/2015 06:18:14, respectively. Their inferred magnitudes are 4.74 and 4.46. The cross-correlation values of *P* and *S* windows are marked to the right.

where N_{obs} is the number of observed aftershocks with $M_b > 4.5$ within 20 d of main shock, and N_{norm} is the number of normalized aftershocks. With $N_{obs} = 13$, we obtain $N_{norm} = 65.2$, which is larger than the mean value of 47.5 for deep earthquakes between 100 km and 350 km in the study of Persh & Houston (2004). In contrast, only six aftershocks with $M_b > 4.5$ were listed in the ANSS catalogue. If we set $N_{obs} = 6$, the corresponding N_{norm} is 30, lower than the mean value.

We also compare the results by calibrating the magnitudes of templates with the ISC catalogue. The corresponding statistical parameters are $M_c = 2.5$, $b = 0.82$, and the Omori's decay rate $P = 0.9$ (Supporting Information Fig. S8). However, the aftershock productivity becomes much lower with $N = 7$ in the first method, and $N_{norm} = 30$ in the second method.

4.6 Search for repeating earthquakes

Because several recent studies have found evidence of repeating earthquakes (i.e. events occurred at virtually the same location with nearly identical waveforms) at intermediate-depth or deep-focus regions (Wiens & Snider 2001; Prieto *et al*. 2012; Yu & Wen 2012), we also conduct an initial search for possible repeating events based on waveforms of the detected events (including all templates). In detail, we search for event pairs with CC > 0.95 (computed with a 16 s time window starting 1 s before the *P* arrival) in vertical components and CC > 0.9 around *S* arrival in horizontal components on at least three stations. We end up getting 15 event pairs, and the total number of repeating earthquakes is about 0.46 per cent of the aftershock sequence. Their recurrence times range from 2 to 15 days. An example of two events with high CC values is shown in

Fig. 7. Their hypocentres are ∼0.4 km apart, within our estimated relative location uncertainty.

5 DISCUSSIONS

5.1 Synthetic tests on earthquake locations

To further test the robustness of our relocation process, we perform two synthetic tests with noise-free and noisy data. The synthetic tests are included in the source code of double-pair DD algorithm (Guo & Zhang 2017). We set the relocated events as 'true' locations, and then calculate the synthetic absolute times with the same 1-D gradient velocity model. Then the synthetic station-pair and double-pair differential times are constructed from the synthetic absolute times. For the noisy synthetic test, Gaussian distributed random noise with zero mean and a standard deviation of 0.6 s is added to the synthetic data, which is estimated from the final residual of the real data inversion and should represent the level of the Gaussian random error in the real data. We then apply the double-pair DD method to the noise-free and noisy data with the same inversion procedure as the real data inversion described above. The median absolute and relative location errors of the synthetic tests are shown in Table 2. Compared to the initial locations with absolute location error of ∼5 km and relative location error of ∼3 km, both absolute and relative locations are much better resolved (Table 2). The relative location uncertainties from the noise-free synthetic test are ∼0.005 km in horizontal and ∼0.02 km in depth, implying double-pair DD location method can achieve high-resolution relative locations with our current event distribution and station coverage. The relative location uncertainties from the noisy synthetic test are ∼0.2 km in horizontal and ∼0.7 km in depth, and have the same order of magnitude as the relative location uncertainties from the bootstrapping analysis for the real data inversion (Table 2), suggesting that our bootstrapping relative location uncertainty estimation for the real data is reliable. The comparable relative location errors from the real data inversion and this noisy synthetic test (Table 2) indicate that relatively large relative location uncertainty for relocated aftershocks, on the order of 0.6 km as compared to ∼0.1 km for the upper-crustal earthquakes in California (Guo & Zhang 2017) is probably due to the large data error. The absolute location errors (error between 'true locations' and relocations) from both of the noise-free and noisy test are ∼1 km in horizontal and ∼2 km in depth, which approximately reflect absolute location uncertainties of the real data inversion.

5.2 The precision of absolute locations

For many earthquake location methods, absolute earthquake locations are difficult to be resolved and rely on the precisions of initial locations. Guo & Zhang (2017) have shown that double-pair DD location method can determine much better absolute locations due to high sensitivity of station-pair data on absolute locations. Their results also showed that the effect from different initial locations is very small for the well-recorded crustal earthquakes in San Andreas Fault. In this study, one primary conclusion is that aftershocks occurred to the west of the main shock. Hence, the precision of absolute locations from double-pair DD location method is very important. To evaluate the sensitivity of double-pair DD location method on absolute locations and the influence of initial locations, we perform two additional tests with different sets of initial locations. The first test is to move the initial locations 0.15° to the east, 0.10° to the south and 5 km shallower, which moves the initial locations in the main-shock slip area. Supporting Information Fig. S9 shows that the relocations moved to the northwest of initial locations. The second test is to move the initial locations further away from the main-shock slip area by 0.15° to the west and 0.15° to the north. The relocations then move to southeast (Supporting Information Fig. S10). Hence, both relocations inverted from two different initial locations tend to move towards our preferred relocations shown in Fig. 5.

Although relocations from different initial locations (Fig 5, and Supporting Information Figs S9 and S10) are not exactly the same, the majority of aftershocks are to the west of the largest main-shock slip, and delineate a near-vertical south-dipping plane. Similarly, when we shift the initial locations in the noisy synthetic tests, the relocations also tend to move back to the 'true' locations (Supporting Information Figs S11 and S12). Based on these tests, we argue that the double-pair DD location method is sensitive to absolute locations and that the absolute locations of our preferred relocations (Fig. 5) are reliable.

5.3 Aftershock sequence and physical mechanism

The Hindu Kush seismic zone is one of the three regions in the world with intensive intermediate-depth earthquake activity in a concentrated volume (Prieto *et al*. 2012; Zarifi & Havskov 2013), also known as the 'earthquake nest'. Pavlis & Hambergur (1991) found that the 1983 M 6.7 intermediate-depth earthquake produced more than 89 aftershocks with M ≥ 3.1 in 34 days, and the aftershock with largest magnitude is smaller than the main shock by 2.6. Our WMFT detected 519 aftershocks with M ≥ 3.1 within the same time period for the 2015 event, and the largest magnitude of aftershocks is 5.8, which is 1.7 smaller than the main-shock magnitude. The 2002 M_w7.4 intermediate-depth earthquake in the Hindu Kush nest have 30 M ≥ 3.1 aftershocks listed in the ANSS catalogue, with largest aftershock 2.9 smaller than main shock in magnitude. All three earthquakes with clear aftershock sequences found by Pavlis & Hambergur (1991) were located very close to the 2015 Hindu Kush earthquake, and with similar focal mechanisms. Because of close locations and similar focal mechanisms to other large intermediate-depth earthquakes, the 2002 M_w7.4 earthquake (and other previous M6–7 events) may also have missing aftershocks. Therefore, we suspect that some large intermediate-depth earthquakes in the Hindu Kush nest might also have abundant aftershock sequences, which can be verified with the same WMFT method in a further study.

As shown in Section 4.5, the aftershock productivity of the 2015 main shock is above the average of deep earthquakes if we use the ANSS magnitudes for the templates, and is below average if the template magnitude is from the ISC catalogue. This shows that the template magnitudes would affect the productivity estimation of detected aftershocks. In this study we mainly focused on results with ANSS catalogue, because the preferred magnitudes in the ISC catalogue are from various resources. Further magnitude calibration could be helpful to produce a catalogue with a unified magnitude scale (Shelly *et al*. 2016), but this is beyond the scope of this paper.

There are several physical models on aftershock generation, such as static and dynamic stresses caused by the main shock, viscoelastic relaxation or fluid diffusion, and afterslip (e.g. Das & Scholz 1981; Freed 2005). Viscoelastic response and fluid diffusion are more plausible to aftershocks at longer time span of months to years (e.g. Freed 2007; Peng & Zhao 2009; Wu *et al*. 2017). Static and dynamic triggering mechanism could be evaluated by comparing the

resulting stress changes and aftershock distributions (King & Deves 2015). Although we did not compute static/dynamic stress changes from the main shock, we found that most aftershocks to the west in the main-shock rupture propagation direction (Fig. 5). This is qualitatively consistent with similar aftershock observations following some large shallow earthquakes (e.g. 1992 M7.3 Landers earthquakes), suggesting that dynamic stress changes likely contribute to triggering aftershocks in the rupture propagation direction.

Many recent studies also invoked post-seismic deformation as the mechanism for driving early aftershocks (Perfettini & Avouac 2004; Peng & Zhao 2009). The direct evidence for afterslip driving aftershocks include consistence of aftershock locations and inverted afterslip from geodetic observations, and aftershock migration following numerical simulation expansion of afterslip (e.g. Kato 2007; Peng & Zhao 2009). Some other observations are considered as supporting evidences of afterslip, including slip deficit of main shock, spatial expansion of aftershocks, and repeating aftershocks (e.g. Wu *et al*. 2017; Yao *et al*. 2017). However, given the large hypocentral depth, it's challenging to detect any post-seismic signals for intermediate-depth earthquakes using ground-based GPS recordings (Boschi *et al*. 2000). As shown in Fig. 5, most aftershocks occurred around the edge of main-shock main slip patch, similar with observations for many large megathrust events (e.g. Hsu *et al*. 2006; Yao *et al*. 2017) or strike-slip events such as the 2004 Parkfield earthquake (Bennington *et al*. 2011). Based on the moderate expansion of aftershock activity with time (Fig. 6b), together with initial observations of repeaters with high similarities (Fig. 7), we hypothesize that afterslip occurred following the 2015 Hindu Kush earthquake and may play a role for driving the aftershock sequence. Further analysis of recurrence times and locations of repeating aftershocks at longer times and stress changes induced by the main shock could shed light on the driving mechanism of the 2015 Hindu Kush aftershocks.

5.4 Implication for main-shock physical mechanisms

Currently there are two widely-accepted candidates for the physical mechanism of intermediate-depth earthquakes: dehydration embrittlement and thermal shear runaway instability (Prieto *et al*. 2012). For dehydration embrittlement, an increase of pore pressure due to existence of fluid would reduce the effective normal stress in depth, resulting in brittle failure events (Green & Houston 1995; Frohlich 2006; Houston 2015). Fluids in subduction zones mainly come from dehydration of subducted sediments or metamorphic phase transition (Houston 2015). Pore fluids also play an important role in aftershock generation following large shallow earthquakes (Nur & Booker 1972; Bosl & Nur 2002). In this study, we found that the expansion mostly occurred immediately following the main shock (Fig. 6). The relatively slow diffusion of water may suggest that other triggering mechanisms are needed to trigger large amount and rapid expansion of aftershocks shortly after the main shock.

In the thermal shear runaway instability model, shear deformation in a strain-weakening shear zone generates ductile creep or melting, thus promoting slip on pre-existing faults (Wiens 2001). Viscous melting has been proposed in some large deep earthquakes such as the 1994 M8.2 Bolivia Earthquake, the second largest deep earthquake ever recorded (Houston 2015; Zhan *et al*. 2014). The energy balance of the initial phase of the 2015 Hindu Kush earthquake is similar to the 1994 Bolivia earthquake, likely indicating occurrence of frictional melting (Houston 2015; Poli *et al*. 2016a). The thermal shear instability model is also compatible with abundant aftershocks (Frohlich 2006) and possible repeating aftershocks (Wiens & Snider 2001; Prieto *et al*. 2012). The short repeating rate of repeaters could be explained by thermal conductive cooling (Wiens & Snider 2001; Yu & Wen 2012). Therefore, thermal instability model might be the cause of the main shock and some aftershocks.

Previous studies showed that the seismicity zone beneath Hindu Kush is dipping to the north between 60–180 km and to different directions below 180 km (Sippl *et al* 2013; Kufner *et al*. 2017). Kufner *et al* (2017) suggested that the overturned seismicity zone beneath Hindu Kush is related to the ongoing India slab breakoff, which splits the slab and seismicity into two different depth domains. Our aftershock distribution is also consistent with the hypothesis that the 2015 Hindu Kush earthquake and other large earthquakes occur in a thin necking shear zone where the slab breaks off (Lister *et al* 2008; Kufner *et al* 2016; Zhan & Kanamori 2016; Poli *et al*. 2016a). Further study of other aftershock sequences and distributions, as well as detection of smaller earthquakes during interseismic period would provide more information on physical mechanisms of intermediate-depth earthquakes in this region.

6 CONCLUSIONS

In this study we used the WMFT to detect 3120 aftershocks within 35 days of the 2015 M_w7.5 Hindu Kush intermediate-depth earthquake, which are more than 15 times the number of events listed in the ANSS catalogue. We found that the aftershock behaviours of the 2015 Hindu Kush event are similar to shallow earthquakes in many aspects, such as relatively high aftershock productivity and a rate decay following the Omori's law. Furthermore, the relocated aftershocks are consistent with the westward propagation of the main-shock rupture (Zhan & Kanamori 2016; Poli *et al*. 2016a), and general observations that most aftershocks occur in the propagation direction of shallow main-shock ruptures (Kilb *et al*. 2003).

ACKNOWLEDGEMENTS

The seismic data of network IU and TJ are obtained from IRIS DMC (http://ds.iris.edu/mda/IU; http://ds.iris.edu/gmap/TJ). We are also grateful to Dr. Jing Wu in Chinese Academy of Sciences and Dr. Xiaofeng Meng in University of Southern California for their help and valuable advice on the matched-filter technique method and analysis of results. CL, ZP and DY are supported by NSF grant EAR-1551022.

REFERENCES

Bennington, N., Thurber, C., Feigl, K.L. & Murray-Moraleda, J., 2011. Aftershock distribution as a constraint on the geodetic model of coseismic slip for the 2004 Parkfield earthquake, *Pure appl. Geophys.,* **168**(10), 1553–1565.

Billington, S., Isacks, B.L. & Barazangi, M., 1977. Spatial distribution and focal mechanisms of mantle earthquakes in the Hindu Kush–Pamir region: a contorted Benioff zone, *Geology,* **5**(11), 699–704.

Boschi, L., Piersanti, A. & Spada, G., 2000. Global postseismic deformation: deep earthquakes, *J. geophys. Res.,* **105**(B1), 631–652.

Bosl, W. & Nur, A., 2002. Aftershocks and pore fluid diffusion following the 1992 Landers earthquake, *J. geophys. Res.,* **107**(B12), ESE 17-1–ESE 17-12.

Brown, J.R., Beroza, G.C. & Shelly, D.R., 2008. An autocorrelation method to detect low frequency earthquakes within tremor, *Geophys. Res. Lett.,* **35**(16), L16305, doi:10.1029/2008GL034560.

Chao, K. *et al.*, 2017. Temporal variation of tectonic tremor activity in southern Taiwan around the 2010 M_L6.4 Jiashian earthquake, *J. geophys. Res.,* **122**(7), 5417–5434.

Chatelain, J.L., Roecker, S.W., Hatzfeld, D. & Molnar, P., 1980. Microearthquake seismicity and fault plane solutions in the Hindu Kush region and their tectonic implications, *J. geophys. Res.,* **85**(B3), 1365–1387.

Das, S. & Scholz, C.H., 1981. Off-fault aftershock clusters caused by shear stress increase?, *Bull. seism. Soc. Am.,* **71,** 1669–1675.

Efron, B. & Gong, G., 1983. A leisurely look at the bootstrap, the jackknife, and cross-validation, *Am. Stat.,* **37**(1), 36–48.

Efron, B. & Tibshirani, R., 1991. Statistics data analysis in the computer age, *Science,* **253,** 390–395.

Frank, W.B. & Shapiro, N.M., 2014. Automatic detection of low-frequency earthquakes (LFEs) based on a beamformed network response, *Geophys. J. Int.,* **197**(2), 1215–1223.

Freed, A., 2005. Earthquake triggering by static, dynamic, and postseismic stress transfer, *Annu. Rev. Earth Planet. Sci.,* **33,** doi:10.1146/ annurev.earth.33.092203.122505.

Freed, A.M., 2007. Afterslip (and only afterslip) following the 2004 Parkfield, California, earthquake, *Geophys. Res. Lett.,* **34,** L06312, doi:10.1029/2006GL029155.

Frohlich, C., 1987, Aftershocks and temporal clustering of deep earthquakes, *J. geophys. Res.,* **92**(B13), 13 944–13 956.

Frohlich, C., 1989, The nature of deep-focus earthquakes, *Annu. Rev. Earth Planet. Sci.,* **17**(1), 227–254.

Frohlich, C., 2006, *Deep Earthquakes,* Cambridge Univ. Press.

Gibbons, S.J. & Ringdal, F., 2006. The detection of low magnitude seismic events using array-based waveform correlation, *Geophys. J. Int.,* **165**(1), 149–166.

Green, H.W. & Houston, H., 1995, The mechanics of deep earthquakes, *Annu. Rev. Earth Planet. Sci.,* **23**(1), 169–213.

Green, H.W. & Marone, C., 2002, Instability of deformation, *Rev. Mineral. Geochem.,* **51**(1), 181–199.

Guo, H. & Zhang, H., 2017, Development of double-pair double difference earthquake location algorithm for improving earthquake locations, *Geophys. J. Int.,* **208**(1), 333–348.

Guo, H., Zhang, H., Nadeau, R.M. & Peng, Z., 2017, High-resolution deep tectonic tremor locations beneath the San Andreas Fault near Cholame, California, using the double-pair double-difference location method, *J. geophys. Res.,* **122**(4), 3062–3075.

Hainzl, S., 2016. Rate-dependent incompleteness of earthquake catalogs, *Seismol. Res. Lett.,* **87**(2A), 337–344.

Hamburger, M.W., Sarewitz, D.R., Pavlis, T.L. & Popandopulo, G.A., 1992, Structural and seismic evidence for intracontinental subduction in the Peter the First range, central Asia, *Bull. geol. Soc. Am.,* **104**(4), 397–408.

Hobbs, B.W. & Ord, A., 1988, Plastic instabilities: Implications for the origin of intermediate and deep focus earthquakes, *J. geophys. Res.,* **93**(B9), 10 521–10 540.

Houston, H., 2015. *Deep Earthquakes, Treatise on Geophysics,* 2nd edn, vol. 4, pp. 329–354.

Hsu, Y. *et al.*, 2006. Frictional afterslip following the 2005 Nias-Simeulue earthquake, Sumatra, *Science,* **312**(5782), 1921–1926.

Iwata, T., 2008. Low detection capability of global earthquakes after the occurrence of large earthquakes: investigation of the Harvard CMT catalogue, *Geophys. J. In.,* **174**(3), 849–856.

Kagan, Y.Y., 2004, Short-term properties of earthquake catalogs and models of earthquake source, *Bull. seism. Soc. Am.,* **94**(4), 1207–1228.

Kagan, Y.Y. & Knopoff, L., 1980, Dependence of seismicity on depth, *Bull. seism. Soc. Am.,* **70,** 1811–1822.

Kato, N., 2007, Expansion of aftershock areas caused by propagating postseismic sliding, *Geophys. J. Int.,* **168,** 797–808.

Kato, A. & Nakagawa, S., 2014. Multiple slow-slip events during a foreshock sequence of the 2014 Iquique, Chile M_w8.1 earthquake, *Geophys. Res. Lett.,* **41**(15), 5420–5427.

Kato, A. & Obara, K., 2014. Step-like migration of early aftershocks following the 2007 M_w6.7 Noto-Hanto earthquake, Japan, *Geophys. Res. Lett.,* **41**(11), 3864–3869.

Kato, A., Obara, K., Igarashi, T., Tsuruoka, H., Nakagawa, S. & Hirata, N., 2012. Propagation of slow slip leading up to the 2011 M_w 9.0 Tohoku-Oki earthquake, *Science,* **335**(6069), 705–708.

Karato, S., Reidel, M.R. & Yuen, D.A., 2001, Rheological structure and deformation of subducted slabs in the mantle transition zone: implications for mantle circulation and deep earthquakes, *Phys. Earth planet. Inter.,* **127**(1–4), 83–108.

Kilb, D., Newman, R.L., Vernon, F.L., Eakins, J.A., Ziegler, L., Bowen, J. & Otero, J., 2003, Education and outreach based on data from the Anza seismic network in Southern California, *Seismol. Res. Lett.,* **74**(5), 522–528.

Kilb, D., Peng, Z., Simpson, D., Michael, A., Fisher, M. & Rohrlick, D., 2012. Listen, Watch, Learn: SeisSound Video Products, *Seismol. Res. Lett.,* **83**(2), 281–286.

King, G.C.P. & Devès, M.H., 2015. Fault interaction, earthquake stress changes and the evolution of seismicity, in *Treatise on Geophysics,* ed. Schubert, G., Oxford, doi:10.1016/B978-0-444-53802-4.00077-4.

Kirby, S.H., Stein, S., Okal, E.A. & Rubie, D.C., 1996, Metastable mantle phase transformations and deep earthquakes in subducting oceanic lithosphere, *Rev. Geophys.,* **34**(2), 261–306.

Kufner, S.-K. *et al.*, 2016, Deep India meets deep Asia: lithospheric indentation, delamination and break-off under Pamir and Hindu Kush (Central Asia), *Earth planet. Sci. Lett.,* **435,** 171–184.

Kufner, S.-K., Schurr, B., Haberland, C., Zhang, Y., Saul, J., Ischuk, A. & Oimahmadov, I., 2017. Zooming into the Hindu Kush slab break-off: a rare glimpse on the terminal stage of subduction, *Earth planet. Sci. Lett.,* **461,** 127–140.

Li, L., Yao, D., Meng, X., Peng, Z. & Wang, B., 2017, Increasing normal-faulting earthquakes in Southern Tibet following the 2015 M_w 7.8 Gorkha, Nepal earthquake, *Tectonophysics,* **714–715,** 63–70.

Lister, G., Kennett, B., Richards, S. & Forster, M., 2008, Boudinage of a stretching slablet implicated in earthquakes beneath the Hindu Kush, *Nat. Geosci.,* **1**(3), 196–201.

Meng, X. & Peng, Z., 2014. Seismicity rate changes in the Salton Sea Geothermal Field and the San Jacinto Fault Zone after the 2010 M_w7.2 El Mayor-Cucapah earthquake, *Geophys. J. Int.,* **197**(3), 1750–1762.

Meng, X., Peng, Z. & Hardebeck, J.L., 2013. Seismicity around Parkfield correlates with static shear stress changes following the 2003 M_w 6.5 San Simeon earthquake, *J. geophys. Res.,* **118**(7), 3576–3591.

Negredo, A.M., Replumaz, A., Villaseñor, A. & Guillot, S., 2007, Modeling the evolution of continental subduction processes in the Pamir-Hindu Kush region, *Earth planet. Sci. Lett.,* **259**(1–2), 212–225.

Nur, A. & Booker, J., 1972. Aftershocks caused by pore fluid flow?, *Science,* **175**(4024), 885–887.

Nyffenegger, P. & Frohlich, C., 2000. Aftershock occurrence rate decay properties for intermediate and deep earthquake sequences, *Geophys. Res. Lett.,* **27**(8), 1215–1218.

Ogawa, M., 1987. Shear instability in a viscoelastic material as the cause of deep focus earthquakes, *J. geophys. Res.,* **92**(B13), 13801–13810.

Pavlis, G.L. & Hamburger, M.W., 1991. Aftershock sequences of intermediate-depth earthquakes in the Pamir-Hindu Kush seismic zone, *J. geophys. Res.,* **96**(B11), 18 107–18 117.

Pegler, G.L. & Das, S., 1998. An enhanced image of the Pamir-Hindu Kush seismic zone from relocated earthquake hypocentres, *Geophys. J. Int.,* **134**(2), 573–595.

Peng, Z. & Zhao, P., 2009. Migration of early aftershocks following the 2004 Parkfield earthquake, *Nat. Geosci.,* **2**(12), 877–881.

Peng, Z., Vidale, J.E., Ishii, M. & Helmstetter, A., 2007. Seismicity rate immediately before and after main shock rupture from high-frequency waveforms in Japan, *J. geophys. Res.,* **112**(B3), 573–595.

Perfettini, H. & Avouac, J.-P., 2004. Postseismic relaxation driven by brittle creep: A possible mechanism to reconcile geodetic measurements and the decay rate of aftershocks, application to the Chi-Chi earthquake, Taiwan, *J. geophys. Res.,* **109**(B2), B02304, doi:10.1029/2003JB002488.

Persh, S.E. & Houston, H., 2004, Strongly depth-dependent aftershock production in deep earthquakes, *Bull. seism. Soc. Am.,* **94**(5), 1808–1816.

Petit, J.P. & Barquins, M., 1988. Can natural faults propagate under Mode II conditions?, *Tectonics,* **7**(6), 1243–1256.

Poli, P., Prieto, G.A., Rivera, E. & Ruiz, S., 2016. Earthquakes initiation and thermal shear instability in the Hindu Kush intermediate depth nest, *Geophys. Res. Lett.*, (4), doi: 10.1002/2015GL067529.

Poli, P. *et al.*, 2016. Complex rupture of the M6.3 2015 March 10 Bucaramanga earthquake: evidence of strong weakening process, *Geophys. J. Int.,* **205**(2), 988–994.

Prieto, G.A., Beroza, G.C., Barrett, S.A., López, G.A. & Florez, M., 2012. Earthquake nests as natural laboratories for the study of intermediate-depth earthquake mechanics, *Tectonophysics,* **570–571,** 42–56.

Prozorov, A.G. & Dziewonski, A.M., 1982. A method of studying variations in the clustering property of earthquakes: application to the analysis of global seismicity, *J. geophys. Res.,* **87**(B4), 2829–2839.

Rayleigh, C.B. & Paterson, M.S., 1965. Experimental deformation of serpentinite and its tectonic implications, *J. geophys. Res.,* **70**(16), 3965–3985.

Roecker, S.W., Soboleva, V., Nersesov, I.L., Lukk, A.A., Hatzfeld, D. & Chatelain, J.L., 1980. Seismicity and fault plane solutions of intermediate depth earthquakes in the Pamir-Hindu Kush region, *J. geophys. Res.,* **85**(B3), 1358–1364.

Ruan, X., Meng, X., Peng, Z., Long, F. & Xie, R., 2017. Microseismic activity in the last five months before the M_w7.9 Wenchuan Earthquake, *Bull. seism. Soc. Am.,* **107**(4), 1582–1592.

Shearer, P.M., 1994, Global seismic event detection using a matched filter on long-period seismograms, *J. geophys. Res.,* **99**(B7), 13 713–13 725.

Shelly, D.R. & Hardebeck, J.L., 2010. Precise tremor source locations and amplitude variations along the lower-crustal central San Andreas Fault, *Geophys. Res. Lett.,* **37**(14), L14301, doi:10.1029/2010GL043672.

Shelly, D.R., Ellsworth, W.L. & Hill, D.P., 2016. Fluid-faulting evolution in high definition: Connecting fault structure and frequency-magnitude variations during the 2014 Long Valley Caldera, California, earthquake swarm, *J. Geophys. Res. Solid Earth,* **121**(3), 1776–1795.

Shelly, D.R., Beroza, G.C. & Ide, S., 2007. Non-volcanic tremor and low-frequency earthquake swarms, *Nature,* **446**(7133), 305–307.

Shelly, D.R., Hill, D.P., Massin, F., Farrell, J., Smith, R.B. & Taira, T., 2013. A fluid-driven earthquake swarm on the margin of the Yellowstone caldera, *J. geophys. Res.,* **118**(9), 4872–4886.

Sippl, C. *et al.*, 2013. Geometry of the Pamir-Hindu Kush intermediate-depth earthquake zone from local seismic data, *J. geophys. Res.,* **118**(4), 1438–1457.

Tang, C.-C., Peng, Z., Chao, K., Chen, C.-H. & Lin, C.-H., 2010. Detecting low-frequency earthquakes within non-volcanic tremor in southern Taiwan triggered by the 2005 M_w8.6 Nias earthquake, *Geophys. Res. Lett.,* **37**(16), L16307, doi:10.1029/2010GL043918.

Vinnik, L.P., Lukk, A.A. & Nersesov, I.L., 1977, Nature of the intermediate seismic zone in the mantle of Pamirs-Hindu-Kush, *Tectonophysics,* **38**(3–4), T9–T14.

Wadati, K., 1928, Shallow and deep earthquakes, *Geophys. Mag.,* **1,** 161–202.

Waldhauser, F. & Ellsworth, W.L., 2000, A double-difference Earthquake location algorithm: method and application to the northern Hayward fault, California, *Bull. seism. Soc. Am.,* **90**(6), 1353–1368

Walter, J.I., Meng, X., Peng, Z., Schwartz, S.Y., Newman, A.V. & Protti, M., 2015. Far-field triggering of foreshocks near the nucleation zone of the 5 September 2012 (M W 7.6) Nicoya Peninsula, Costa Rica earthquake, *Earth planet. Sci. Lett.,* **431,** 75–86.

Wiemer, S., 2001, A software package to analyze seismicity: ZMAP, *Seismol. Res. Lett.,* **72**(3), 373–382.

Wiens, D.A., 2001. Seismological constraints on the mechanism of deep earthquakes: temperature dependence of deep earthquake source properties, *Phys. Earth planet. Inter.,* **127**(1–4), 1463–1466.

Wiens, D.A. & Snider, N.O., 2001. Repeating deep earthquakes: evidence for fault reactivation at great depth, *Science,* **293**(5534), 1463–1466.

Wiens, D.A., McGuire, J.J., Shore, P.J., Bevis, M.G., Draunidalo, K., Prasad, G. & Helu, S., 1994. A deep earthquake aftershock sequence and implications for the rupture mechanism of deep earthquakes, *Nature,* doi:10.1038/372540a0.

Woessner, J. & Wiemer, S., 2005, Assessing the quality of earthquake catalogues: estimating the magnitude of completeness and its uncertainty, *Bull. seism. Soc. Am.,* **95**(2), 684–698.

Wu, J., Yao, D., Meng, X., Peng, Z., Su, J. & Long, F., 2017. Spatial-temporal evolutions of early aftershocks following the 2013 M_w6.6 Lushan earthquake in Sichuan, China, *J. geophys. Res.,* **122**(4), 2873–2889.

Yamanaka, Y. & Shimazaki, K., 1990. Scaling relationship between the number of aftershocks and the size of the main shock, *J. Phys. Earth,* **38**(4), 305–324.

Yao, D., Walter, J.I., Meng, X., Hobbs, T.E., Peng, Z., Newman, A.V., Schwartz, S.Y. & Protti, M., 2017. Detailed spatiotemporal evolution of microseismicity and repeating earthquakes following the 2012 M_w7.6 Nicoya Earthquake, *J. geophys. Res.,* **122**(1), 524–542.

Ye, L., Lay, T., Zhan, Z., Kanamori, H. & Hao, J., 2016. The isolated ~680 km deep 30 May 2015 M_w7.9 Ogasawara (Bonin) Islands earthquake, *Earth planet. Sci. Lett.,* **433,** 169–179.

Yu, W.-C. & Wen, L., 2012. Deep-focus repeating earthquakes in the Tonga-Fiji subduction zone, *Bull. seism. Soc. Am.,* **102**(4), 1829–1849.

Zarifi, Z. & Havskov, J., 2003. Characteristics of dense nests of deep and intermediate-depth seismicity, *Adv. Geophys.,* **46,** 237–278.

Zhan, Z., 2017. Gutenberg-Richter law for deep earthquakes revisited: a dual-mechanism hypothesis, *Earth planet. Sci. Lett.,* **461,** 1–7.

Zhan, Z. & Kanamori, H., 2016. Recurring large deep earthquakes in Hindu Kush driven by a sinking slab, *Geophys. Res. Lett.,* **43**(14), 7433–7441.

Zhan, Z., Kanamori, H., Tsai, V. C., Helmberger, D. & Wei, S., 2014. Rupture complexity of the 1994 Bolivia and 2013 Sea of Okhotsk deep earthquakes, *Earth Planet. Sci. Lett.,* **385,** 89–96.

Zhang, M. & Wen, L., 2015. An effective method for small event detection: match and locate (M&L), *Geophys. J. Int.,* **200**(3), 1523–1537.

SUPPORTING INFORMATION

Supplementary data are available at *GJI* online.

Figure S1. (a) Cross-correlation peaks of a detected event 20151026113055 at vertical component of each station and the stacked trace: red traces are *P*-wave windows, and blue traces are *S*-wave windows. (b) Waveforms of two events 20150604065301 and 20150608032812 with cross-correlation higher than 0.75 in a time window of [−1 2] s around *P* arrival, differential times are marked as dt, and the cross-correlation values are on the right.

Figure S2. 1-D velocity model of Vp from Sippl *et al.* (2013) (blue) and 1-D velocity model used in this study (black).

Figure S3. M5.32 event detected on 2015 October 26, the template is 20151112235356.

Figure S4. Magnitude difference versus the median amplitude ratios between the templates and detected events that are also listed in the ANSS catalogue.

Figure S5. (a) Magnitude versus logarithmic time of detected events using threshold 12 × MAD, red dots are templates, black circles are detected events and the red solid line marks the Mc = 2.7. (b) Frequency–magnitude dependence for detected aftershocks generated by ZMAP, and the red dashed line indicates the result of 'Best Combination'. (c) Cumulative number of aftershocks in 35 d after the main shock, compared with the Omori–Utsu prediction.

Figure S6. (a) Time–magnitude for the detected aftershock and corresponding event within 6 s on the ISC catalogue, the event pairs are connected by red dashed lines. All the aftershocks within 35 d of main shock on ISC catalogue are plotted here. (b) Magnitude difference of the same event detected and in ISC catalogue. (c) The common events in ANSS and ISC catalogue and their magnitude within 35 d of main shock. (d) Magnitude difference of the same event in ANSS and ISC catalogue.

Figure S7. Relocated aftershocks in our study and Kufner *et al.* (2017) in (a) map view, (b) depth-longitude view and (c) depth-latitude view. Grey dots are background seismicity from Kufner *et al.* (2017).

Figure S8. (a) Magnitude versus logarithmic time of detected events according to the ISC catalogue, red dots are templates, black circles are detected events and the red solid line marks the Mc = 2.5. (b) Frequency–magnitude dependence for detected aftershocks generated by ZMAP, and the red dashed line indicates the result of 'Best Combination'. (c) Cumulative number of aftershocks in 35 d after the main shock, compared with the Omori–Utsu prediction.

Figure S9. Same as Figs 5 (a)–(d) in main text for relocated aftershocks after shifting the initial locations 0.15° to the east, 0.1° to the south and 5 km shallower. Red circles are initial locations.

Figure S10. Same as Figs 5(a)–(d) in main text for relocated aftershocks after shifting the initial locations 0.15° to the west and 0.15° to the north. Red circles are initial locations.

Figure S11. Noisy synthetic test after shifting the initial locations 0.15° to the east, 0.1° to the south and 5 km shallower. Red circles are initial locations.

Figure S12. Noisy synthetic test after shifting the initial locations 00.15° to the west and 0.15° to the north. Red circles are initial locations.

Table S1. Example of an event on ISC catalogue with different magnitudes from different sources.

Movie S1. The 'earthquake sound' of aftershocks within an hour of the 2015 M_w7.5 Hindu Kush earthquake.

Li_etal_2017_Hindu_Kush_Detect.cat.txt

Li_etal_2017_GJI_relocated_5km.cat.pdf

Please note: Oxford University Press is not responsible for the content or functionality of any supporting materials supplied by the authors. Any queries (other than missing material) should be directed to the corresponding author for the paper.